JOURNAL OF COMPUTATIONAL PHYSICS 115, 366–375 (1994)

Boundary Element Analysis of the Time-Dependent Motion of a Semi-infinite Bubble in a Channel

D. HALPERN*

Department of Biomedical Engineering, Northwestern University, Evanston, Illinois 60208

AND

D. P. GAVER, III

Department of Biomedical Engineering, Tulane University, New Orleans, Louisiana 70118

Received April 13, 1992; revised February 17, 1994

We present a boundary element method to investigate the time-dependent translation of a two-dimensional bubble in a channel of width 2a containing a fluid of viscosity μ and surface tension γ. In our analysis, the flow rate, Q^*, is specified, and the finger progresses forward at a nonconstant velocity until it reaches a steady-state velocity U^*. The primary dimensionless parameter in the unsteady formulation is $Ca_0 = \mu Q^*/2a\gamma$, representing the ratio of viscous forces to surface-tension forces. Steady-state results are given in terms of the conventional form of the capillary number, $Ca_U = \mu U^*/\gamma$. The steady-state shape of the finger, the pressure drop across the tip of the finger, and its radius of curvature are presented for a range of Ca_U much larger than has previously been published ($0.05 \leq Ca_U \leq 10^4$). Good agreement is shown to exist with the finite-difference results of Reinelt and Saffman in the range of their studies ($0.05 \leq Ca_U \leq 3$), and with the experimental data of Tabeling *et al.* whose studies extend to $Ca_U = 0.2$. Beyond $Ca_U = 20$, we predict that the steady-state meniscus interface shape is insensitive to Ca, and that the pressure drop is directly proportional to a viscous pressure scale. A regression analysis of the finger width (β) versus Ca_U yields $\beta \approx 1 - 0.417(1 - \mathrm{Exp}(-1.69\, Ca_U^{0.5025}))$, which gives the correct behavior for both small and large Ca_U. This regression result may be considered an extension of the low-capillary asymptotic predictions of Bretherton, who found a $Ca_U^{2/3}$ dependence for Ca very small ($Ca_U < 0.02$). The result of this regression analysis is consistent with Taylor's measurements of residual film thickness in circular tubes, which shows a $Ca_U^{1/2}$ dependence for values of $Ca_U < 0.09$.

1. INTRODUCTION

Convection of a finger of air through a viscous fluid contained between two narrowly spaced plates has been studied by numerous investigators since Saffman and Taylor published the results of their fundamental investigation in 1958 [23]. This problem, two-phase flow in a Hele–Shaw cell, is of basic interest for several reasons. First, the averaged two-dimensional velocity u of the viscous fluid between the plates (averaged in the transverse direction) follows an equation that is analogous to Darcy's law for flow through porous media. This system has been used to study phenomena related to the recovery of oil from oil fields and the transport of substances in porous media [1]. In experiments using Hele–Shaw cells, it was observed that as the meniscus interface progressed forward, the planar interface became unstable and formed a fingered interface. As the fingers progressed, one finger was found to dominate and develop into a stable finger. Saffman and Taylor [23], and Pitts [17] found experimentally that the stable finger has a lateral width equal to one-half of the cell width ($\lambda = \frac{1}{2}$) in the limit of large capillary number, $Ca_U = \mu U^*/\gamma$, where μ is the fluid viscosity, U^* is the steady-state finger velocity, and γ is the interfacial surface tension. The lateral finger width was found to increase with decreasing Ca_U. The study of this fingering behavior has been of interest to investigators of interfacial stability, dendritic crystal growth and the formation of fractal structures. Recently, flow in a flexible-walled Hele–Shaw cell has been suggested as a model that may simulate the reopening of closed pulmonary airways [8].

In their analyses of two-phase displacement in a Hele–Shaw cell, Saffman and Taylor [23] found closed-form solutions to the lateral interface shape by neglecting the influence of surface tension. However, they were unable to determine the value of λ corresponding to this large capillary number limit. Nevertheless, given a value of λ close to $\frac{1}{2}$, the analytical solutions provided lateral interface profiles that are in good agreement with experimental observations. When surface tension effects due to lateral curvature were included, McLean and Saffman [15] were able to predict values of λ whose dependency on the capillary number agreed qualitatively with experiments, and they predicted a value of $\lambda = \frac{1}{2}$ in the limit of large Ca_U.

* Current address: Department of Mathematics, University of Alabama, Tuscaloosa, Alabama 35487.

0021-9991/94 $6.00

However, these solutions do not agree quantitatively with measurements of λ for small and intermediate values of Ca_U. Subsequently, Romero [22] and Vanden-Broeck [28] found different solutions to the model studied by McLean and Saffman [15]. However, Tanveer [26] has shown that only the solutions provided by McLean and Saffman [15] are stable. DeGregoria and Schwartz [5] used time-dependent computational simulations to trace the behavior of small disturbances in the finger tip. The results of these calculations also indicate that McLean and Saffman's solutions are stable. When noise was added to the system, the otherwise stable finger bifurcated continuously to produce a simple tree-structure [6]. For large values of the capillary number, it was also discovered that instability occurs without the addition of noise.

Although the addition of surface tension effects due to lateral curvature allows for the prediction of the finger width λ, this prediction is only qualitatively accurate. In particular, experimental measurements of λ for a given value of the stability parameter, $1/B = 12\, Ca_U (w/a)^2$, are larger than those predicted by the two-dimensional analyses described above. Here w/a is the ratio of the Hele–Shaw cell width to transverse thickness. It has been suggested that the discrepancy between the measured and predicted values of λ may be due to three-dimensional effects created by variation of curvature in the transverse direction. The models described above assumed that the driving fluid completely expelled the driven fluid from between the plates and, thus, that the interface curvature in the transverse direction was constant [15]. However, measurements by Tabeling, Zocchi, and Libchaber [25] indicate that the thickness of the residual film, or alternatively the transverse finger shape, depends on the capillary number. Additionally, by conducting experiments in cells of differing aspect ratios (w/a), they found that the single stability parameter $1/B$ was insufficient to uniquely describe the lateral finger width. This, too, was attributed to three-dimensional effects.

Several investigators have calculated the thickness of the film left behind after a finger of air pushes through the viscous fluid. Asymptotic solutions for transverse finger shape and pressure drop in two-phase displacement in a Hele–Shaw cell have been solved by Park and Homsy [16] and are accurate for flows in which the capillary number is small ($Ca_U < 0.02$) and in which inertia is negligible. This problem has also been investigated computationally by Reinelt and Saffman [21], who used an adaptive-grid composite-mesh finite difference scheme and gave results for values of Ca_U in the range $0.01 \leq Ca_U \leq 3.0$. However, in this range of Ca_U, the finger width increases monotonically with Ca_U, a behavior that is unlikely to continue for large values of Ca_U.

To date, computational investigations have focussed on the steady-state behavior of a bubble progressing through a channel. The aim of the present investigation is to compute the *time-dependent* transverse finger shape and pressure drop in two-phase displacement in a channel. In addition, we aim to extend the range of capillary numbers investigated to values beyond those of previous studies ($Ca_U < 10^4$). We use an efficient numerical method to solve the Stokes equations for two-dimensional slow viscous flows whereby the velocity and stress fields are expressed in terms of one-dimensional integrals, thereby reducing storage and computational work compared with that required in finite-difference or finite-element methods. The numerical implementation of this scheme is called the *boundary element method*, which has been used to solve linear elasticity problems [3], the Stokes equations [9, 18] and surface flows in which nonlinearities enter through the stress-jump condition at the interface between two fluids. Examples include the deformation and burst of bubbles and drops [14, 19] and rigid particles approaches deformable interfaces [2, 11]. A major difficulty with this method lies in the fact that fundamental solutions of the Stokes equations are singular, and consequently analytical methods [9, 12], special Gaussian quadrature rules [3], or expansions about the singularities [10, 13] are needed to integrate these boundary integrals. We will follow the approach taken by Youngren and Acrivos [29] and Rallison and Acrivos [19] and express the integrals in terms of the velocity and stress fields as opposed to the streamfunction–vorticity approach taken by Lu and Chang [12]. The other major difference from [12] is that our method can be applied to problems with time-dependent boundary conditions.

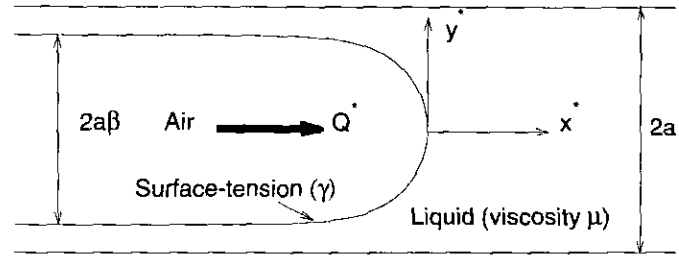

FIG. 1. Two-phase displacement in a Hele–Shaw cell. Flow rate, Q^*, is used to displace viscous fluid with gas-phase finger.

2. PROBLEM FORMULATION

2.1. *Governing Equations*

In this model problem we consider the *time-dependent* motion of an infinitely long air finger being driven forward by a constant flow rate Q^*. The bubble moves through a channel of width $2a$ filled with an incompressible Newtonian fluid of viscosity μ (Fig. 1). The steady-state finger tip velocity is given by $U^* = Q^*/(2a\beta)$, where $2a\beta$ is the upstream finger width. We will neglect the dynamics of the inviscid air-phase and assume that the air pressure is constant. The governing equations are scaled as

$$\mathbf{u}^* = \frac{Q^*}{2a}\mathbf{u}, \quad p^* = \frac{\gamma}{a}p, \quad \mathbf{x}^* = a\mathbf{x}, \quad t^* = \frac{2a^2}{Q^*}t, \tag{2.1}$$

and $\quad h^* = a\,h,$

where * represents a dimensional quantity, $\mathbf{u} = (u, v)$ is the fluid velocity, p is the pressure, γ is the surface tension of the air–liquid interface, and $y = h(x, t)$ is the position of the air–liquid interface. With this scaling, the non-dimensional Navier–Stokes equations are

$$\nabla p = Ca_Q \nabla^2 \mathbf{u} - Ca_Q \cdot \mathrm{Re}\,(\mathbf{u}_t + (\mathbf{u}\cdot\nabla)\,\mathbf{u}), \tag{2.2}$$

where the subscript t denotes differentiation with respect to time, $Ca_Q = \mu Q^*/(2a\gamma)$ is the capillary number based on the imposed constant flow rate representing the relative magnitude of the viscous to interfacial forces, and $\mathrm{Re} = \rho Q^*/(2\mu)$ is the Reynolds number. For slow viscous flow, $Ca_Q \cdot \mathrm{Re} \ll 1$, and the fluid equations for the liquid phase may be approximated by the non-dimensional Stokes equations, given by

$$\nabla p = Ca_Q \nabla^2 \mathbf{u}. \tag{2.3}$$

In addition, the continuity equation must also be satisfied:

$$\nabla \cdot \mathbf{u} = 0. \tag{2.4}$$

For a given bubble shape, we fix our reference frame to a frame that moves forward with the associated meniscus velocity (which depends upon β), and thus the no-slip conditions at the channel walls are

$$\mathbf{u} = -\frac{\mathbf{e}_x}{\beta} \quad \text{at } y = \pm 1, \tag{2.5}$$

where $\mathbf{e}_x = (1, 0)$ is the unit vector in the horizontal direction. Far ahead of the finger we impose Poiseuille flow,

$$\mathbf{u} \to \left(\frac{1}{2Ca_Q}\frac{\partial p}{\partial x}(y^2 - 1) - \frac{1}{\beta}\right)\mathbf{e}_x \quad \text{as } x \to \infty, \tag{2.6}$$

and behind the finger we specify that

$$\mathbf{u} \to \frac{-\mathbf{e}_x}{\beta} \quad \text{as } x \to -\infty. \tag{2.7}$$

Then by mass conservation we require that

$$\frac{\partial p}{\partial x} \to -3\,Ca_Q \quad \text{as } x \to \infty. \tag{2.8}$$

At the air–liquid interface, we apply the stress jump condition

$$[\sigma \cdot \mathbf{n}] = \mathbf{n}\nabla \cdot \mathbf{n}, \tag{2.9}$$

where [ ] denotes the jump in normal stress across the air–liquid interface, $\sigma = -p\mathbf{I} + Ca_Q\,(\nabla_{\mathbf{u}} + \nabla\mathbf{u}^T)$ is the stress tensor, $\mathbf{n}$ is the outward unit normal, and $\nabla \cdot \mathbf{n}$ is the surface curvature. In addition, the kinematic boundary condition specifies that the interface moves normal to itself at the local normal velocity,

$$\frac{\partial \mathbf{Y}}{\partial t} \cdot \mathbf{n} = \mathbf{u} \cdot \mathbf{n} \quad \text{at } y = h(x, t), \tag{2.10}$$

where $\mathbf{Y} = \mathbf{Y}(x, y, t)$ is the interfacial position vector. This condition is used to time-step the finger domain and, thus, introduces the time-dependent motion into our solution. Steady-state solutions are determined when the normal component of the interfacial velocity approach zero. The velocity boundary conditions, (2.5)–(2.7) instantaneously adjust to changes in finger width β. When "continuous" boundary conditions are applied (see Table 1), the interface point DE is forced to move with the neighboring point.

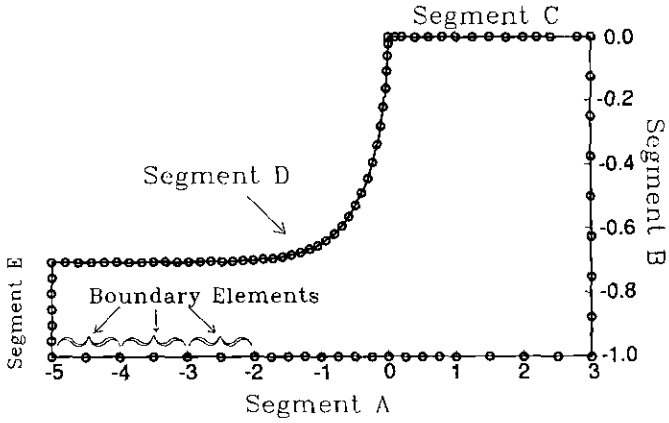

FIG. 2. Boundary discretization used for the computational simulation. Boundary conditions for segments A, B, C, D, and E are described in Table I.

2.2. *The Boundary Element Method*

A solution for the velocity field resulting from Stokes flow (2.3) can be obtained in terms of single and double layer potentials by taking Fourier transforms of (2.3) and (2.4) and applying Green's theorem [10],

$$\mathbf{u}_k(\mathbf{x}) = \int_S \mathbf{T}_{ik}(\mathbf{x}, \mathbf{y})\mathbf{u}_i\, dS_y - \frac{1}{Ca}\int_S \mathbf{U}_{ik}(\mathbf{x}, \mathbf{y})\tau_i\, dS_y, \tag{2.11}$$

where

$$\mathbf{U}_{ik}(\mathbf{x}, \mathbf{y}) = -\frac{1}{4\pi}\left\{\delta_{ik}\log|\mathbf{x} - \mathbf{y}| - \frac{(x_i - y_i)(x_k - y_k)}{|\mathbf{x} - \mathbf{y}|^2}\right\},$$
$$\mathbf{T}_{ik}(\mathbf{x}, \mathbf{y}) = -\frac{1}{\pi}\frac{(x_i - y_i)(x_j - y_j)(x_k - y_k)}{|\mathbf{x} - \mathbf{y}|^4}n_j(\mathbf{y}), \tag{2.12}$$

S represents the boundary surface (Fig. 2) and $\tau_i = \sigma_{ij}n_j$, where i,j are indices that are either 1 (x-direction) or 2 (y-direction).

In the limit as $\mathbf{x}$ tends to a point on the boundary surface, due to the singular nature to the integrands, the solution (2.11) becomes

$$\mathbf{C}_{ki}\mathbf{u}_i(\mathbf{x}) = \int_S \mathbf{T}_{ik}(\mathbf{x}, \mathbf{y})\mathbf{u}_i \, dS_y - \frac{1}{Ca}\int_S \mathbf{U}_{ik}(\mathbf{x}, \mathbf{y})\tau_i \, dS_y, \quad (2.13)$$

where $\mathbf{x} \in S$. The tensor $\mathbf{C}_{ki}$ is due to the jump in stress at the surface. It has a value of $\frac{1}{2}\,\delta_{ki}$ if the boundary is smooth but has a more complicated structure if the domain has corners [3]. The known values of τ_i in (2.13) are given by Eq. (2.9).

The numerical procedure used to solve (2.13) involves discretizing the boundary (Fig. 2) into N 3-point elements, so that Eq. (2.13) is approximated by

$$\mathbf{C}_{ki}\mathbf{u}_i(\mathbf{x}) - \sum_{j=1}^{N}\int_{S_j} \mathbf{T}_{ik}(\mathbf{x}, \mathbf{y})\mathbf{u}_i \, dS_y = -\frac{1}{Ca}\sum_{j=1}^{N}\int_{S_j} \mathbf{U}_{ik}(\mathbf{x}, \mathbf{y})\tau_i \, dS_y. \quad (2.14)$$

The variables $\mathbf{u}$ and τ are written in terms of quadratic polynomials, ϕ_j, which are functions of a local coordinate ξ ($-1 \leq \xi \leq 1$),

$$\begin{pmatrix} u \\ v \end{pmatrix} = \sum_{j=1}^{3} \phi_j(\xi)\begin{pmatrix} u_j \\ v_j \end{pmatrix}$$
$$\begin{pmatrix} \tau_x \\ \tau_y \end{pmatrix} = \sum_{j=1}^{3} \phi_j(\xi)\begin{pmatrix} \tau_{x_j} \\ \tau_{y_j} \end{pmatrix} \quad (2.15)$$

where (u_j, v_j) and (τ_{x_j}, τ_{y_j}) are the velocities and stresses at the node point j on the surface. $\phi_j(\xi)$ are given by

$$\phi_1 = \frac{1}{2}\,\xi(\xi - 1), \quad \phi_2 = (1 - \xi)(1 + \xi), \quad \phi_3 = \frac{1}{2}\,\xi(1 + \xi). \quad (2.16)$$

Similarly, x and y are written in terms of ϕ_j at each node point:

$$\begin{pmatrix} x \\ y \end{pmatrix} = \sum_{j=1}^{3} \phi_j(\xi)\begin{pmatrix} x_j \\ y_j \end{pmatrix}. \quad (2.17)$$

Equation (2.14) can then be written as a system of linear equations,

$$\mathbf{Hw} = \mathbf{Gt}, \quad (2.18)$$

where $\mathbf{H}$ and $\mathbf{G}$ are respectively $4N \times 4N$ and $4N \times 6N$ matrices, and $w_{2j-1} = u_j$, $w_{2j} = v_j$, $t_{2j-1} = \tau_{x_j}$, $t_{2j} = \tau_{y_j}$ for $j = 1, \ldots, 2N$. Matrix $\mathbf{G}$ is larger than $\mathbf{H}$ in order to allow the stress vector to have two distinct values at corner points, thus accounting for the two possible orientations of the normal vector at corner points. As will be shown in the next section, this is particularly useful at corner points, where the normal to the surface abruptly changes direction. The elements of $\mathbf{H}$ and $\mathbf{G}$ are obtained using a 10-point regular Gaussian quadrature if $\mathbf{x}$ is not coincident with one of the node points of S_j. Otherwise a logarithmic quadrature is incorporated to compute those portions of the integrals in (2.14) that contain the logarithmic singularity. The diagonal coefficients of $\mathbf{H}$ are computed indirectly by imposing a uniform flow in both the x and y directions. This is a much simpler, but accurate, technique than using highly specialized methods to compute the principal value of $\mathbf{H}$ [3]. We then apply the boundary conditions (2.5)–(2.9) to (2.14), as described below in *Implementation Considerations*, and rearrange the system so that

$$\mathbf{Az} = \mathbf{f}, \quad (2.19)$$

where $\mathbf{A}$ is a $4N \times 4N$ matrix, $\mathbf{z}$ is a $2N$ vector containing the unknown velocities and stresses and $\mathbf{f}$ contains the known stress or velocity information.

System (2.19) is solved using Gaussian elimination with partial pivoting. $\mathbf{z}$ can be uniquely determined if the shape of the boundary is known so that the curvature in (2.9) can be computed. Our scheme is similar to that used by Martinez [13] in that we assume an initial shape, which does not satisfy the steady-state condition $\mathbf{u} \cdot \mathbf{n} = 0$ on the finger, and solve for $\mathbf{z}$. The new shape is computed by applying the kinematic boundary condition and determining the new $\mathbf{z}$ by solving (2.19) again. This procedure is repeated sequentially until $|\mathbf{u} \cdot \mathbf{n}| < \boldsymbol{\varepsilon}$, where $\boldsymbol{\varepsilon} \ll 1$. We use the initial value solver lsoda from ODEPACK which uses either Adams–Bashforth method for non-stiff systems or Gear's method for stiff systems. In all our computations we have selected our steady-state criterion to be $\boldsymbol{\varepsilon} = 0.001$, which we found sufficient to ensure convergence. An additional check on convergence was performed by computing the pressure difference across the finger tip using two independent methods. This is discussed in the next section.

We calculate profiles for different values of the capillary number sequentially. When this is done, the solution for the previous capillary number is used as an initial condition for the next simulation. In so doing, the maximum normal velocity may be quite small initially; then it increases in magnitude and finally decreases toward zero as the meniscus approaches its steady-state configuration. In order to ensure that the meniscus approaches steady-state, we set a criterion such that the simulation must progress to $t \geq 5$ before calculating the value of $\mathbf{u} \cdot \mathbf{n}$ for use in satisfying the steady-state criterion described above.

2.3. *Implementation Considerations*

As described by (2.9) the normal-stress jump across an air–liquid interface is proportional to the interfacial curvature, $\kappa = \nabla \cdot \mathbf{n}$, and thus the solution to this model problem requires

TABLE I

Description of the "Continuous" and "Mixed" Boundary Conditions

	Boundary segment									
Boundary conditions	A $-5 \le x \le 3$, $y = -1$	AB $x = 3$, $y = -1$	B $x = 3$, $-1 \le y \le 0$	BC $x = 3$, $y = 0$	C $0 \le x \le 3$, $y = 0$	CD $x = 0$, $y = 0$	D $-5 \le x \le 0$, $y = h(x,t)$	DE $x = -5$, $y = -1 + \beta$	E $x = -5$, $-1 \le y \le -1 + \beta$	EA $x = -5$, $y = -1$
Continuous	$u = -1/\beta$ $v = 0$	$u = -1/\beta$ $v = 0$	$u = 1.5(1 - y^2) - 1/\beta$ $v = 0$	$u = 1.5 - 1/\beta$, $\tau_{1,C} = 0$ $v = 0$	$\tau_1 = 0$ $v = 0$	$\tau_{1,C} = 0$, $\tau_{1,D} = \kappa n_1$, $v = 0$, $\tau_{2,D} = \kappa n_2$	$\tau_1 = \kappa n_1$ $\tau_2 = \kappa n_2$	$\tau_{1,D} = \kappa n_1$, $u = -1/\beta$, $\tau_{2,D} = \kappa n_2$, $v = 0$	$u = -1/\beta$ $v = 0$	$u = -1/\beta$ $v = 0$
Mixed	$u = -1/\beta$ $v = 0$	$\tau_{1,A} = -3 \cdot Ca_Q$, $v = 0$, $u = -1/\beta$, $\tau_{2,B} = 3 \cdot Ca_Q$	$u = 1.5(1 - y^2) - 1/\beta$ $\tau_2 = -3Ca_Q \cdot y$	$u = 1.5 - 1/\beta$, $\tau_{2,B} = 0$, $\tau_{1,C} = 0$, $v = 0$	$\tau_1 = 0$ $v = 0$	$\tau_{1,C} = 0$, $v = 0$, $\tau_{1,D} = \kappa n_1$, $\tau_{2,D} = \kappa n_2$	$\tau_1 = \kappa n_1$ $\tau_2 = \kappa n_2$	$\tau_{1,D} = \kappa n_1$, $\tau_{1,E} = 0$ $\tau_{2,D} = \kappa n_2$, $\tau_{2,E} = 0$	$\tau_1 = 0$ $\tau_2 = 0$	$\tau_{1,E} = 0$, $\tau_{1,A} = 0$ $\tau_{2,E} = 0$, $\tau_{2,A} = 0$

an accurate determination of the interfacial curvature. The curvature was computed at each interfacial node i by

$$\kappa_i = (x_{SS})_i (y_S)_i - (x_S)_i (y_{SS})_i, \tag{2.20}$$

where the subscript s denotes differentiation with respect to the arc-length s. The arc-length to each node (s_i) was computed by integrating along the interface using a quadratic spline approximation to the interface shape. Cubic splines were then computed for x_i vs s_i and y_i vs s_i, with specified end derivative conditions to ensure symmetry. These were then differentiated to compute κ_i.

We used a non-uniform distribution of points along the interface since the accurate calculation of the curvature is crucial to the precise computation of the normal-stress balance and since the curvature changes rapidly near the meniscus nose. For this study, we selected a distribution such that $\Delta s_i = i^{3/2} s_{\text{total}}/M^{3/2}$, where $i = 1$ denotes the nose, $i = M$ specifies the last point on the finger, s_{total} is the total meniscus arc-length, and Δs_i is the arc-length from node i-1 to node i.

As time-stepping progresses, the meniscus moves in a direction normal to its surface, and thus the nose can progress away from $x = 0$. In order to eliminate the possibility of the nose tip (the intersection of segments C and D in Fig. 2) from overtaking the neighboring point in segment C, we move the points along segments C and B with the same horizontal velocity as the nose point. This serves to hold the boundary element spacing constant near the meniscus nose. Periodically (typically every $\Delta t = 0.25$), we redistribute the domain by sliding the meniscus such that the nose once again resides at the origin (moving segments C and B in conjunction), and then redistributing the interface points such that they satisfy the spacing distribution described above.

Although the formulation presented in Section 2.1 provides a well-posed mathematical statement of the problem, ambiguity exists in its translation to the boundary element formulation. Table I defines two plausible sets of boundary conditions for this problem. The first set of conditions is called "continuous," since at corners AB and EA the conditions specify velocities (u, v), and the unknowns are thus the stresses (τ_1, τ_2) at the corner. The second set of boundary conditions takes advantage of the fact that our computational method permits discontinuous stress vectors at the juncture of any two boundary elements; we use this capability at domain cornerpoints. As mentioned above, this stress-vector discontinuity is a result of the discontinuity in the normal vector at the corners and has no other physical significance. This set of conditions we call "mixed," since the corner point conditions are in all cases a mixture of velocity and stress conditions, with the unknowns being 2 (of the 4) stresses on the corner node as described in Table I. For example, at the corner node AB (the intersection of boundary segment A with boundary segment B), the "mixed" condition case specifies the x-component of stress on segment A ($\tau_{1,A}$), the y-component of stress on segment B ($\tau_{2,B}$), and the velocity components (u, v). The unknowns are thus $\tau_{1,B}$ (the x-component of stress on the B-side of the corner), and $\tau_{2,A}$ (the y-component of stress on the A-side of the corner).

Figure 3 shows the results of the calculation of the normal stress (τ_2) along the bottom wall using the "continuous" and "mixed" boundary conditions. This figure shows that both formulations provide similar stresses in the middle of the domain, but the "continuous" boundary conditions provide erratic results near the endpoints. This behavior is due to stress discontinuities created by normal vector discontinuities at boundary corners. For example, along segment A the normal vector is $\mathbf{n}_A = (0, -1)$ so $\tau_{1,A} = -Ca_Q(\partial u/\partial y + \partial v/\partial x)$. As $x \to \infty$, $\tau_{1,A} \to -3 \cdot Ca_Q$. However, along segment B the normal vector is $\mathbf{n}_B = (1, 0)$ so $\tau_{1,B} = -p + 2\, Ca_Q\, (\partial u/\partial x) = -p$. This discontinuity is not permitted by continuous boundary conditions, which thus leads to the errors demonstrated by Fig. 3. The computations described in the remainder of this paper were therefore computed using the "mixed" conditions presented in Table I.

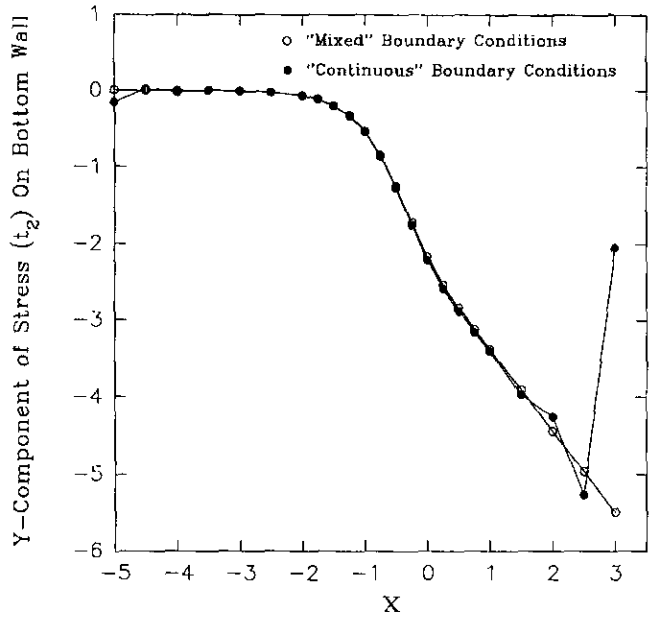

FIG. 3. Computed values of the normal-stress (t_2) along the bottom wall for $Ca_Q = 0.35$: O = mixed boundary conditions; ● continuous conditions.

In addition, the horizontal component of velocity at the finger tip is an unknown, since at the intersection of segments C and D, we can set $\tau_{1,C} = 0$ and $v = 0$ along the axis of symmetry and $\tau_{i,D} = \kappa n_i$ along the curved segment. The other unknown here is $\tau_{2,C}$. This enables us to compute the pressure difference across the finger tip using two methods. Since $p = 2Ca_Q \partial u/\partial x - \tau_{1,D}$, p can be determined by approximating $\partial u/\partial x$ using finite differences along the centerline. Also, $\tau_{2,C} = -p + 2\,Ca_Q\,\partial v/\partial y$, so that $p = -(\tau_{1,D} + \tau_{2,C})/2$, which eliminates the need for any further approximations. By comparing these estimates of p, we can infer the accuracy of our solution near this highly-important region. We find that when the estimates of p differ by less than 1%, our point density is sufficient near the tip.

3. RESULTS

3.1. *Convergence*

The global error of the temporal behavior was investigated by time-stepping the simulation with different tolerance magnitudes for the norm of the local error. The computational method assessed the local error norm as the max (E_i/W_i), where E_i is the absolute value of the error estimate evaluated by the difference between the predictor and corrector steps solutions, W_i is the $\max(|Y_i|, 1)$, and Y_i is the magnitude of the solution at the ith point. We simulated the transition behavior from a $Ca_Q = 0.35$ steady-state meniscus to a $Ca_Q = 1.25$ steady-state profile using tolerance criteria of 10^{-3}, 10^{-5}, and 10^{-7}. From these results, we found that the global error was small for local tolerance values greater than or equal to 10^{-5}, and we use 10^{-5} for all future calculations.

We explored the influence of the domain size by varying the endpoints over the range $-7 \le x \le 7$ to $-2 \le x \le 0.25$ while holding the domain point density fixed for $Ca_Q = 0.3$ and $Ca_Q = 1.0$. We found that the results (tip curvature, pressure drop, and β) were insensitive to the domain size for domains larger than $-3 \le x \le 1$. For the remainder of the calculations, the domain size was set to $-5 \le x \le 3$.

We investigated the sensitivity of the time-dependent behavior to the node-point redistribution interval ($\Delta t_{\text{redistribute}}$) by calculating the transition from a $Ca_Q = 0.35$ profile to a $Ca_Q = 1.25$ profile using redistribution intervals of $\Delta t_{\text{redistribute}} = 0.1$, 0.25, and 1.0. We deduced from these results that the error induced by node-point redistribution is negligible if $\Delta t_{\text{redistribute}} \le 0.25$.

Convergence as a function of the spatial distribution of node points on the air–liquid interface was examined by computing steady-state profiles for $Ca_Q = 0.35$ and $Ca_Q = 1.25$ profiles with various numbers of nodes defining the air–liquid interface (segment D in Fig. 2). In these computations the number of interfacial points varied from 14 to 50, and all other node points

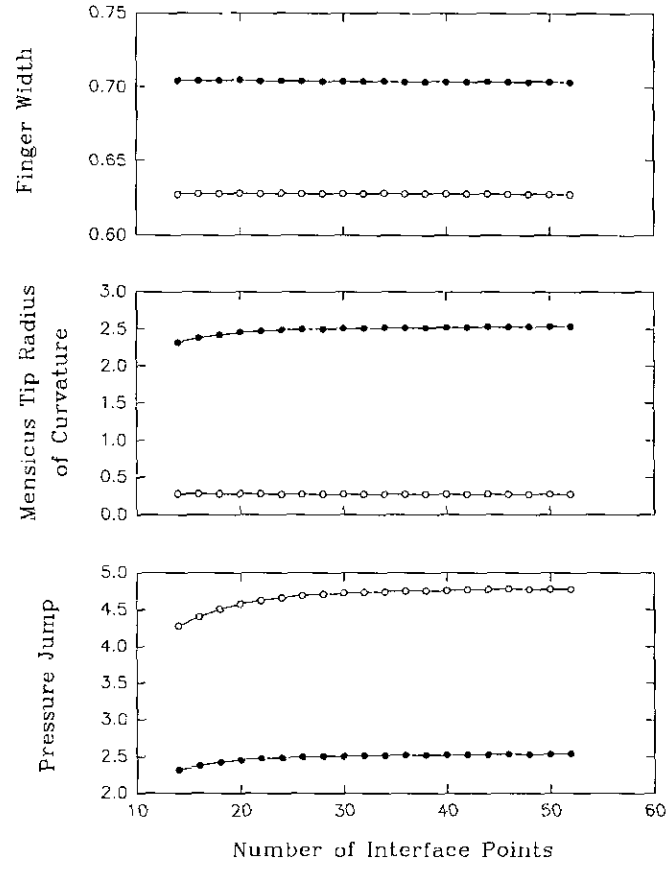

FIG. 4. Dependence of computational prediction of finger width (β), finger radius of curvature, and interfacial pressure jump on the number of interface points: ●, $Ca_Q = 0.35$; O, $Ca_Q = 1.25$.

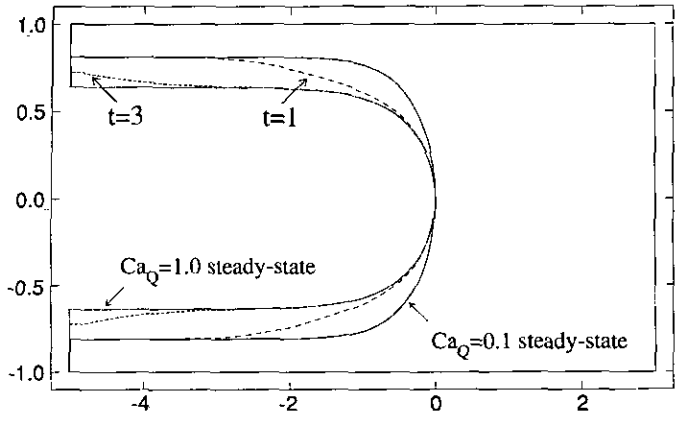

FIG. 5. Time-dependent transition from the steady-state finger shape for $Ca_Q = 0.1$ to the steady-state finger shape for $Ca_Q = 1.0$ due to an incremental change in the flow rate at $t = 0$.

were held constant in the same configuration as shown in Fig. 2. Steady-state convergence was assumed to occur when max $(\mathbf{u} \cdot \mathbf{n})_{\text{interface}} \leq 0.001$ (discussed below). The results of this study are shown in Fig. 4, which presents plots of the finger width (β), tip curvature, and the pressure jump as a function of the number of node points. While the tip curvature and pressure jump are more sensitive than β to the number of interfacial points, all cases converge to values independent of the number of interface points if at least 25 interface points are used. This figure suggests, however, that high capillary number simulations may require an increased number of interface points if convergence is to be accomplished. For this reason, our simulations of problems with $0.7 \leq Ca_Q < 4$ incorporate 40 interface points, and 66 points for $Ca_Q \geq 4.0$. As we will show, the meniscus shape becomes insensitive to the capillary number for $Ca_Q > 6$, and thus a greater number of interfacial points is unnecessary for simulations of flows with $Ca_Q > 6$.

3.2. *Time-Dependent Behavior*

Figure 5 shows the time-dependent behavior of the meniscus interface when Ca_Q is increased from 0.1 to 1.0 (for instance, by incrementing the flow rate). Initially the maximum normal velocity is quite small and the shape of the interface changes by a small amount. The curved tip approaches its steady shape quite rapidly ($t \approx 2$) but it takes another three time units for a thin-film region to stabilize. Capillary waves, which dampen out with time, can be observed to propagate upstream of the tip to the thin film.

Figure 6 details the change in bubble geometry as a function of time resulting from a step increment of Ca_Q from 0.1 to 1.0. As indicated by Fig. 5, the bubble tip changes shape more rapidly than the film region. The upstream film thickness changes shape as a capillary wave sweeps through the film. Figure 6 also presents the time-dependent behavior of the maximum interfacial normal velocity (max$(\mathbf{u} \cdot \mathbf{n})$). These data indicate that steady state occurs when max$(\mathbf{u} \cdot \mathbf{n}) < 0.001$. This value will be assumed for our steady-state predictions below.

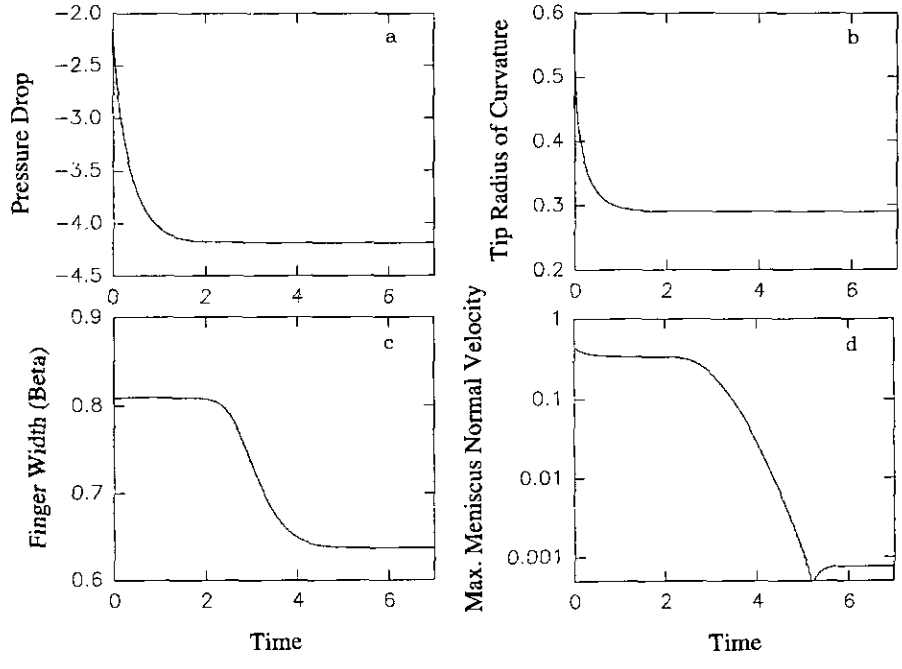

FIG. 6. Plots of (a) ΔP, (b) R_{tip}, (c) finger width, and (d) max$(\mathbf{u} \cdot \mathbf{n})$ versus time due to an instantaneous change in Ca_Q from $Ca_Q = 0.1$ to 1. The values at $t = 0$ correspond to the steady-state values for $Ca_Q = 0.1$.

3.3. *Steady-State Behavior*

In order to compare the results from our simulations with results from computational and experimental studies by other investigators, we present the steady-state results in terms of the steady-state capillary number, $Ca_U = Ca_Q/\beta = \mu U^*/\gamma$. Figure 7a shows that the thickness of the uniform film left behind the tip, $1-\beta$, increases with increasing Ca_U and tends to a constant as $Ca_U \to \infty$. For small Ca_U, Bretherton [4] showed that

$$\begin{aligned} \beta &\to 1 - 1.337\, Ca_U^{2/3} \quad \text{as } Ca_U \to 0, \\ \Delta P &\to 1 + 3.8\, Ca_U^{2/3} \quad \text{as } Ca_U \to 0. \end{aligned} \tag{3.1}$$

Bretherton's [4] asymptotic predictions, adapted for the 2D Hele–Shaw problem (Park and Homsy [16]), are shown in Fig. 7a,b. Also, the results of Reinelt and Saffman's finite-difference calculations [21] are shown as solid lines in these figures. Reinelt and Saffman [21] have shown that their calculations agree with those of Bretherton [4] for $Ca_U < 0.02$, establishing a limit for the validity of the asymptotic approach. Ratulowski [20] extended the results of Bretherton [4] by using a more accurate form of lubrication theory throughout the gap region. His values of β agree quite well with those of Reinelt and Saffman [21] for Ca_U of almost 0.5, but the pressure drop across the finger tip is underestimated even at $Ca_U \approx 0.1$. As can be seen from Figs. 7a,b,c, our steady-state results agree with the finite-difference computations of Reinelt and Saffman [21] to the limit of their calculations ($Ca_U = 3$). Figures 6 and 7a–c show that the finger shape becomes more slender and the tip curvature increases with increasing Ca_U. Using the boundary element method, we extended calculations of this system to values of $Ca_U = 10^4$, well beyond those of previous studies. The results of this investigation show that the finger radius of curvature has a minimum value of $R = 0.25$ at approximately $Ca_U = 20$; then it increases slightly and approaches a constant radius of curvature of $R = 0.278$ at values of $Ca_U > 100$. Likewise, the finger width, β, approaches a constant value of 0.580 for values of $Ca_U > 100$. The dimensionless pressure jump, $\Delta P^*/(\gamma/a))$ becomes directly proportional to Ca_U for values of $Ca_U > 100$: $\Delta P^*/(\gamma/a)) \approx Ca_U$. Thus, the dimensional pressure jump, ΔP^*, becomes proportional to $\mu U/a$, a quantity that represents the viscous shear stress. This result is reasonable, since for values of $Ca_U > 100$ the meniscus shape is essentially fixed, and thus the increased pressure drop must be due purely to viscous forces in the neighborhood of the meniscus. Experimental replication of the large Ca_U predictions will require Re to be quite small ($Re \ll Ca_U^{-1}$). This may be possible using fluids that are highly viscous, or in Hele–Shaw cells whose transverse dimension (a) is very small.

Tabeling *et al.* [25] measured the residual film that remained after finger penetration in Hele–Shaw cells of various aspect ratios for values of $Ca_U \leq 0.2$. A regression of the residual film, d, vs, Ca_U for each value of the aspect ratio, w/a, of the form

$$d = d_\infty (1 - e^{-BCa_U^{2/3}}) \tag{3.2}$$

was found to provide a reasonable fit to the experimental data over the range of $0 < Ca_U < 0.2$. Equation (3.2) was chosen since it reduces to the relationship determined by Bretherton's analysis for values of $Ca_U \ll 1$. This regression formula was generalized by Tabeling for all values of w/a with the regression form

$$\frac{d_{\max}}{b} = 0.119(1 - e^{-0.019(w/a)})(1 - e^{-8.58Ca_U^{2/3}}), \tag{3.3}$$

or

$$\beta = 1 - 0.238(1 - e^{-0.019(w/a)})(1 - e^{-8.58Ca_U^{2/3}}). \tag{3.4}$$

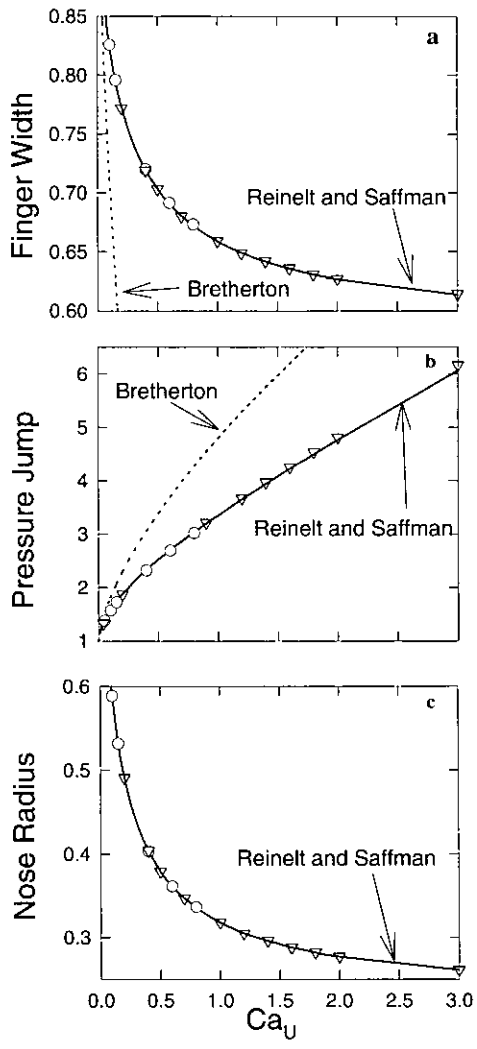

FIG. 7. Predictions of steady state (a) finger width, (b) ΔP, and (c) meniscus radius of curvature. BEM: ○ = 28 pts, ∇ = 40 pts. Lines represent results from Bretherton (1961) and Reinelt and Saffman (1985).

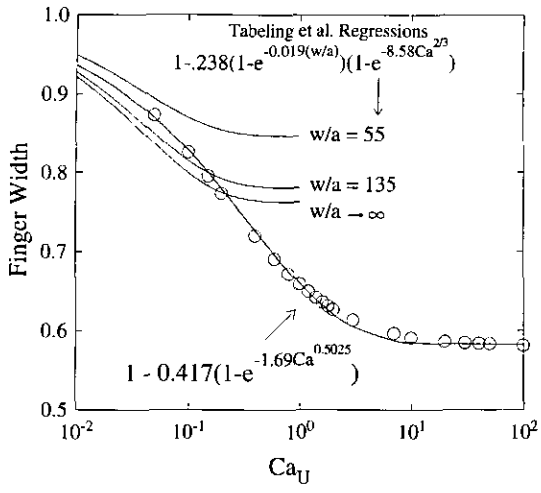

FIG. 8. Comparison of the finger width predictions with the empirically derived regressions of Tabeling *et al.* [25]. ○ represents predictions from boundary element simulations.

In Fig. 8, we plot Eq. (3.4) for values of w/a that correspond to several of the aspect ratios investigated by Tabeling *et al.* [25]. In addition, we plot (3.4) in the limit of $(w/a) \to \infty$. Finally, we plot the predictions of β from our numerical computations for the two-dimensional ($w/a = \infty$) Hele–Shaw cell. This figure shows that for $Ca_U < 0.15$, Eq. (3.4) fits our predictions well. However, beyond $Ca_U = 0.15$, these regressions plateau, while our predictions show β continuing to decrease, and thus a large discrepancy between (3.4) and our predictions of β arises for $Ca_U > 0.15$. Nevertheless, the general form of (3.4) provides a relationship that resembles the results of our numerical simulations. We thus generalized this form with an arbitrary power of Ca_U and regressed it to our computational predictions over the range of $0.05 \leq Ca_U \leq 100$ using a Marquardt–Levenberg algorithm. The resulting regression formula is

$$\beta = 1 - 0.417(1 - e^{-1.69Ca_U^{0.5025}}). \tag{3.5}$$

This regression, shown in Fig. 8, has an error norm of 0.026 and clearly provides a good fit to the computational predictions. This regression shows that the finger width and, hence, the film thickness, varies almost exactly with $Ca_U^{1/2}$ for small values of Ca_U. However, as the capillary number increases, the Ca_U dependence dampens exponentially. This regression result may be considered to be an extension of the low-capillary asymptotic predictions of Bretherton [4], who found a $Ca_U^{2/3}$ dependence for small values of Ca_U ($Ca_U < 0.02$). Our regression analysis result is very similar to the film thickness relationship proposed by Fairbrother and Stubbs [7] and Taylor [27], based upon their experiments of two-phase flow in cylindrical tubes.

4. CONCLUSIONS

In this paper we have presented a method for investigating time-dependent two-phase flow in a channel and have detailed a number of important implementation considerations that must be considered in order to produce accurate results. In particular, we find that it is necessary for corner-point boundary conditions to be specified so as to provide for discontinuous stresses in the region where the unit outward normal is discontinuous. This implementation also has the added benefit of allowing time-dependent boundary conditions.

The boundary element method was found to be capable of simulating two-phase displacement in a channel for a range of capillary numbers much larger than those of previous studies ($0.05 \leq Ca_U \leq 10^4$). The steady-state results of these simulations are in excellent agreement with those of Reinelt and Saffman [21], who used a multiple-grid finite-difference approach, for values of the capillary number in the range of their study ($Ca_U \leq 3.0$). This agreement validates our numerical method. We found the interesting result that, for values of $Ca_U > 20$, the steady-state meniscus shape is insensitive to Ca_U. In this region, the pressure varies directly with a viscous scale ($\mu U/a$) and not the capillary pressure scale (γ/a). This finding is identical to the pressure scaling assumed by Martinez and Udell [14] in their analysis of bubbles flowing through tubes. An additional new result is that the radius of curvature attains its minimum at $Ca_U \approx 20$.

A regression analysis of the finger width (β) versus Ca_U shows that $\beta \approx 1 - 0.417(1 - \text{Exp}[-1.69\, Ca_U^{0.502}])$. In the limit of $Ca_U \ll 1$, this regression result is in agreement with the experimental results of Taylor [27], who studied two-phase displacement in capillary tubes for values of $Ca_U < 0.09$. However, as the capillary number increases, we find that the Ca_U dependence dampens exponentially. While our low Ca_U simulations agree with the asymptotic predictions of Bretherton [4] (valid for $Ca_U < 0.02$), the $\text{Exp}(-1.69Ca_U^{1/2})$ regression result may be considered as an extension of the asymptotic result, valid for $O(1)$ values of Ca_U.

The constancy of β for large values of Ca_U may be responsible for diminishing the three-dimensional nature of two-phase displacement in a Hele–Shaw cell, which may explain why a two-dimensional analysis of the system (one that neglects the transverse finger geometry) accurately predicts the lateral finger width (λ) for large values of Ca_U. Given the success of the boundary element method for the time-dependent solution of this problem, we hope to apply this technique to more complex problems with more than one free surface, such as the steady and unsteady flows of bubbles through channels with compliant walls.

ACKNOWLEDGMENTS

This research was funded by the Whitaker Foundation, NSF Grants BCS-9358207, and BCS-9209558, and NIH Grant HL51334. D.P.G. is a Parker B. Francis Fellow of Pulmonary Research. We appreciate the help provided

by D. A. Reinelt. D. Halpern wishes to acknowledge support by Prof. J. B. Grotberg, Northwestern University, through NSF Grant CTS-9013083.

REFERENCES

1. P. M. Adler and H. Brenner, *Annu. Rev. Fluid Mech.* **20,** 35 (1988).
2. E. P. Ascoli, Ph.D. thesis, California Institute of Technology, 1988.
3. C. A. Brebbia and J. Dominguez, *Boundary Elements—An Introductory Course* (Comput. Mech., Southampton, 1989).
4. F. P. Bretherton, *J. Fluid Mech.* **10,** 166 (1961).
5. A. J. DeGregoria and L. W. Schwartz, *J. Fluid Mech.* **164,** 383 (1986).
6. A. J. DeGregoria and L. W. Schwartz, *Phys. Fluids* **28**(8), 2313 (1985).
7. F. Fairbrother and A. E. Stubbs, *J. Chem. Soc.* **1,** 527 (1935).
8. D. P. Gaver III, R. W. Samsel, and J. Solway, *J. Appl. Physiol.* **69**(1), 74 (1990).
9. M. A. Kelmanson, *J. Eng. Math.* **17,** 329 (1983).
10. O. A. Ladyzhenskaya, *The mathematical theory of viscous incompressible flow* (Gordon & Breach, New York, 1963).
11. S. H. Lee and L. G. Leal, *J. Colloid Interface Sci.* **87,** 81 (1982).
12. W. Q. Lu and H. C. Chang, *J. Comput. Phys.* **77,** 340 (1988).
13. M. J. Martinez, Ph.D. thesis, University of California, Berkley, 1987.
14. M. J. Martinez and K. S. Udell, *J. Appl. Mech.* **56,** 211 (1989).
15. J. W. McLean and P. G. Saffman, *J. Fluid Mech.* **102,** 455 (1981).
16. C.-W. Park and G. M. Homsy, *J. Fluid Mech.* **139,** 291 (1984).
17. E. Pitts, *J. Fluid Mech.* **97,** 56 (1980).
18. C. Pozrikidis, *J. Fluid Mech.* **180,** 495 (1987).
19. J. M. Rallison and A. Acrivos, *J. Fluid Mech.* **89,** 191 (1978).
20. J. Ratulowski, Ph.D. thesis, University of Houston, 1988.
21. D. A. Reinelt and P. G. Saffman, *SIAM J. Sci. Statist. Comput.* **6,** 542 (1985).
22. L. Romero, Ph.D. thesis, California Institute of Technology, 1982.
23. P. G. Saffman and G. I. Taylor, *Proc. R. Soc. London A* **245,** 312 (1958).
24. H. A. Stone and L. G. Leal, *J. Fluid. Mech.* **198,** 399 (1989).
25. P. Tabeling, G. Zocchi, and A. Libchaber, *J. Fluid Mech.* **177,** 67 (1987).
26. S. Tanveer, *Phys. Fluids* **30**(3), 651 (1987).
27. G. I. Taylor, *J. Fluid Mech.* **10,** 161 (1961).
28. J. M. Vanden-Broeck, *Phys. Fluids* **26,** 2033 (1983).
29. G. K. Youngren and A. Acrivos, *J. Fluid Mech.* **69,** 377 (1975).